

2D MXene Electrochemical Transistors

Min-A Kang^{1,3,†}, Jyoti Shakya^{1†}, Jian Li¹, Armin VahidMohammadi⁵, Weiqian Tian^{1,4*}, Erica Zeglio^{1*}, Mahiar Max Hamed^{1,2*}

¹ Department of Fibre and Polymer Technology, KTH Royal Institute of Technology, Teknikringen 56, 10044 Stockholm, Sweden

² Wallenberg Wood Science Center, Teknikringen 56, 10044 Stockholm, Sweden

³ Department of Materials Science and Engineering, Northwestern University, Evanston, IL 60208, USA

⁴ School of Materials Science and Engineering, Ocean University of China, Qingdao, Shandong 266100, China

⁵ A. J. Drexel Nanomaterials Institute and Department of Materials Science and Engineering, Drexel University, Philadelphia, PA 19104, USA

[†] Equal contribution

* E-mail: mahiar@kth.se, zeglio@kth.se, tianweiqian@ouc.edu.cn

Abstract

The solid-state field-effect transistor, FET, and its theories were paramount in the discovery and studies of graphene. In the past two decades another transistor based on conducting polymers, called the organic electrochemical transistor (ECT) was shown and largely studied. The main difference between ECTs and FETs is the mode and extent of channel doping: while in FETs the channel only has surface doping through dipoles, the mixed ionic-electronic conductivity of the channel material in Organic ECTs enable bulk electrochemical doping. As a result, the organic ECT maximizes conductance modulation at the expense of speed. Until now ECTs have been based on conducting polymers, but here we show for the first time that MXenes, a class of 2D materials beyond graphene, have mixed ionic-electronic properties that enable the realization of electrochemical transistors (ECTs). We show that the formulas for organic ECTs can be applied to these 2D ECTs and used to extract parameters like mobility. These MXene ECTs have a high transconductance values but low on-off ratios. We further show that conductance switching data measured using ECT in combination with other in-situ ex-situ electrochemical measurements, is a powerful tool for correlating the change in conductance to that of redox state: to our knowledge this is the first report of this important correlation for MXene films. Many future possibilities exist for MXenes ECTs, and we think other 2D materials with bandgaps can also form ECTs with single or heterostructured 2D materials. 2D ECTs can draw great inspiration and theoretical tools from the field of organic ECTs and have the potential to considerably extend the capabilities of transistors beyond that of conducting polymer ECTs, with added properties such as extreme heat resistance, tolerance for solvents, and higher conductivity for both electrons and ions than conducting polymers.

Keywords: two-dimensional materials, self-assembly, electrochemical transistor, electrochromism, iontronic devices

1. Introduction

The discovery of the basic electronic behavior of one-atom-thick graphene in 2004 [1] gave rise to two important directions in materials science: the field of physics in two-dimensional (2D) materials, and the realization of a future roadmap of 2D materials beyond graphene. Additionally, one of the most important technical advances in 2D materials has been the discovery that layered crystals can be exfoliated and colloidally stabilized in liquids, enabling their fabrication from polar solvents, such as water [2]. Computational studies have predicted that thousands of materials can exfoliate into 2D materials [3]; a number that is driven up by the contribution of scientific technologies. Among them, transitional metal dichalcogenides (TMDs) and transition metal carbides and/or carbonitrides labeled MXenes [4] currently comprise the large classes of 2D materials beyond graphene. TMDs and MXenes introduce many new capabilities not present in graphene, such as tunable bandgaps and conductivity, and high pseudocapitance [5, 6].

The electronic behavior of graphene was initially studied using field effect transistors (FETs) [1]. FETs constitute the building block of computers and therefore nano-engineered 2D materials have been pursued as an alternative to metal-oxide-

semiconductor FETs (MOSFETs) in complementary metal-oxide semiconductor (CMOS) [7]. In FETs, the induced dipole moments at the dielectric layer generated by the application of a gate bias modulate the electrical field and conductivity across the channel. The FET as a three-terminal device also opened the path towards another form of transistor popularized in the past two decades: the organic electrochemical transistor (ECT) [8]. In contrast to the conventional dielectric used in FETs, ECTs include an electrolyte between the channel and gate. The main difference between ECTs and FETs is the mode and extent of channel doping: while in FETs the channel only has surface doping through dipoles, the mixed ionic-electronic conductivity of the channel material in Organic ECTs enable bulk electrochemical doping [9]. As a result, the organic ECT maximizes conductance modulation at the expense of speed [10]. Conjugated polymers are the most common ECT materials, with conductance switching generated by modulation of their redox state upon doping. [11] The most dominant organic ECT material to date is poly(3,4-ethylenedioxythiophene):polystyrene sulfonate (PEDOT:PSS), due to its stability in water and ambient condition, large capacitance, and high ionic conductivity. PEDOT:PSS operation hinges on the decrease of conductance through depletion of mobile holes upon cation injection [12]. While PEDOT:PSS represents the most prominent example of a p-type organic conductor, n-type materials have emerged in the past decade, driven by the need to increase device complexity and sensitivity for biosensors. In contrast to p-type materials, in n-type semiconductors the conductivity is provided by the formation of mobile electrons upon cation injection [13]. ECTs based on conducting polymers have been extensively studied and applied to several fields: electronic textiles [14], biology [15] displays, and neuromorphic computers [10, 16]. However, the demonstration of ECTs based on 2D materials has yet to be explored.

We recently described that 2D titanium carbide ($\text{Ti}_3\text{C}_2\text{T}_x$) MXene films change their bulk electronic conductivity at low operating voltages (similar to doping in conducting polymers) and used 2D MXene to realize electrochemical random access memories (ECRAMs) [17]. Our results showed that MXene films could act as mixed with ion-electron conductors for this specific application. Here we considerably advance this work by proposing that these MXene devices indeed belong to the larger class of ECT devices. We further evaluate the impact of controlled MXene thin film formation on the redox properties and mixed ionic/electronic conductivity of films, by fabricating the ECTs using both layer-by-layer (LbL) assembly and spin-coating for the multilayer films. We further show that the theories for ECTs can be applied for MXenes, and make, to our knowledge the first experiments, that elucidate the switching mechanism of MXene in ECTs using spectro-electrochemistry combined with electronic device data.

2. Results and discussion

2.1 Fabrication of multi-layered 2D MXene and characterization

Ultrathin 2D $\text{Ti}_3\text{C}_2\text{T}_x$ MXene films have been used to fabricate field-effect transistors (FETs) [18]. However, to achieve the bulk charge capacity needed for ECTs, we need to go beyond single/few layers. This requires implementing scalable methods to form unique multilayered stacks, ranging from tens to several hundred layers. To obtain the best possible performance in terms of electronic conductivity, these layered films should form well-ordered stacks so that adjacent 2D layers have appropriate geometrical sizes and maximum interfacial contact. Moreover, to provide high capacitance, the chemical functionalities and spacing between the 2D flakes should be tailored for efficient ion transport and ion-electron coupling. We have previously shown that directed layer-by-layer (LbL) self-assembly of 2D materials, in which no polymer but only a small charged molecule is used between the layers, is a viable option for fabricating multi-layered 2D materials with volumetric capacitance up to 583 F cm^{-3} [19]. In short, this method relies on the deposition of alternating layers of oppositely charged materials from an aqueous solution at room temperature. A positively charged substrate is immersed in a solution of negatively charged 2D material flakes leading to the formation of a very thin layer, held together by electrostatic adsorption. Further immersion in a solution of a positively charged molecule reverses the surface charge enabling the deposition of another layer of 2D material. The process is repeated n times to form n -layered films. In this study, we used an aqueous solution of tris(3-aminopropyl)amine (TAPA) at pH 7.5 for the controlled fabrication of 2D $\text{Ti}_3\text{C}_2\text{T}_x$ MXene multilayers. We compared this fabrication method with spin-coated MXene films to better understand the impact of controlled layer formation on the redox properties and mixed ionic/electronic conductivity of the films. During the sample preparation, the minimum thickness that we could achieve for spin-coated films to fully and homogeneously cover the substrate was 5 times, whereas we could achieve films with a minimum thickness already for 3 bi-layers of LbL-assembled films. For the fabrication of all MXene films, we used a dispersion of MXene at 2 g L^{-1} in water (Figure 1a). Field Emission Scanning Electron Microscope (FESEM) images display representative cross-sectional images for both spin-coated (Figure 1b) and LbL-assembled (Figure 1c) MXene on Si substrates. These images show that films produced via LbL-assembly with $n = 20$ exhibit higher thickness and layers organization with respect to films prepared by subsequent spin coating steps (20 in total, see experimental section for details). We previously used FESEM images to extract the thicknesses of LbL-assembled MXene films, and extrapolated a thickness growth of around 9 nm per bi-layer

[17]. The linear growth, as a function of n , allowed us to use LbL-assembly for fabrication of thin films with variable, precisely controlled thicknesses.

2.2 Spectroelectrochemical analysis

We performed in-situ UV-vis-NIR spectroelectrochemistry to characterize the electrochromic properties of the MXene films either spin-coated or LbL assembled on indium tin oxide (ITO) coated glass using a 1M PVA/H₂SO₄ gel electrolyte (Figure 2a, see the experimental section for details). We used a silver pellet as our pseudo reference electrode to match the electrochemical potential between the spectroelectrochemical and the electrochemical transistor measurements (described in section 2.3). UV-vis-NIR spectroscopy of Ti₃C₂T_x MXene thin films exhibits several characteristic features depending on the fabrication method. The UV-Vis-NIR spectra of spin-coated MXene films exhibit a broad absorption spectrum, with a continuous increase of absorbance from the near-IR region to the UV attributed to the inter-band transitions [20] and a shoulder at around 760 nm (Figure 2b). In contrast, LbL-assembled MXenes exhibit a distinct band with a maximum at 761 nm attributed to surface plasmons, i.e., the collective oscillations of free charge carriers (electrons) [21]. Increasing the number of spin-coating steps leads to a minor increase in the absorption at 760 nm with respect to the local maximum at $\lambda < 450$ nm (Figure S1). Whereas, the data for LbL-assembled films (Figure 2c, 2d) show that the magnitude of the absorption maximum increases from 3 to 10 MXene layers, corroborating FESEM data on the higher level of organization provided by the LbL method. Data for the spin coated films showed very small changes, with a decrease in absorption over the whole spectral window, upon application of cathodic biases from 0 V to -0.8V.

In contrast, layer-by-layer films which are held together by TAPA in-between the layers, exhibited a much larger change in absorption spectra for potentials below -0.8 V. The local maximum below 600 nm exhibited a decrease in intensity, while the maximum at 760 nm showed a decrease in intensity and blue shift to 670 nm (at -0.8 V). This phenomenon has previously been attributed to a change in the electron density of MXene, which in turn leads to a change in surface plasmon resonance [22]. Moreover, we observed an increase in absorption at wavelengths above 900 nm with the formation of an isosbestic point, indicating the protonation of Ti=O functionalities on MXene surface to Ti-OH in presence of strong acids, changing the oxidation state of Ti, and electron density [22-24]. Similar effects were previously observed for (MXene/TAPA) [19].

Spectroelectrochemical data at anodic potentials to 0.6 V, however, show an irreversible decrease in absorption over the whole spectral window, which may be attributed to irreversible oxidation of Ti₃C₂T_x (Figure S2) [22, 25]. Larger changes could be observed for the films deposited via layer-by-layer assembly, which could be attributed to a disruption of the electrostatic interaction between the layers upon intercalation of sulfonate groups at oxidative potentials [26]. The latter two phenomenon need further future studies to increase the lifetime of devices.

2.3 MXene ECTs

Because of the two combined facts: i) that Lbl films allowed controlled growth contrary to spin-coated pure MXene films, and ii) that the LbL/TAPA films showed larger changes in UV-Vis absorption spectra for potentials in the range of 0 to -0.8 V, than pristine MXene films, we focused our attention to fabricating ECT devices using these LbL films. To fabricate ECT devices, we used gold as electrode contacts with channel dimensions of 20 μ m length and 1000 μ m width. LbL coated films were used as the channel material. We used 1 M H₂SO₄/poly(vinyl alcohol) (PVA) as the gel electrolyte and a silver pellet as the gate (Figure 3a, see experimental section for details).

The output and transfer characteristics for transistors with varying channel thickness based on number of LbL layers are presented in Figures 3b-3e. We have also shown device to device variability in supporting information (Figure S3). Photos of ECTs with LbL films of various thickness are shown in figure S4. Output curves exhibit a linear ohmic behavior, consistent with the metallic character of MXene (Fig S5). The output and transfer characteristics show that MXene operates at positive drain voltages, consistent with the n-type transport of MXene films.

The ECTs switched ON at $V_{TH} = 0.85$ V (determined using extrapolation in the linear region method (ELR) method) and the conductance of MXene was proportional to gate voltages in the range of 0 V to 1 V. In these transistors g_m is the transconductance defined as the derivative of channel current as a function of gate voltage ($\partial I_D / \partial V_G$). The maximum transconductance $g_{m,max}$ was 2.89 mS for $n=3$ layers and $g_{m,max} = 0.75$ mS. for $n=10$.

Although organic ECTs are different from FETs, it has been shown that the same equation as those used to describe electronic charge transport in long-channel FETs can be used for organic ECTs in steady-state [27-29]. Specifically, the equation that describes transfer characteristics in a regime where doping occurs everywhere in the channel [29] is given by:

$$g_m = \frac{wd}{L} \mu C_v (V_G - V_{TH}) \quad (1)$$

Here g_m is the transconductance, V_{TH} is the threshold voltage, V_G is the gate voltage, and W (width), d (thickness), and L (length) are the channel dimensions. C_v is volumetric capacitance, and μ is the mobility of electrons (or holes).

The main difference between the equation for ECTs and FETs is that the transconductance in ECTs scales with the thickness and not just the channel area (i.e., W and L). This distinction arises since field-effect only modulates the channel at the semiconductor-insulator interface whereas redox doping modulates the carrier density throughout the bulk of the ECT channel. Importantly, Figure 4a shows that for the same channel geometry of $L = 20 \mu\text{m}$ and $W = 1000 \mu\text{m}$, the areal capacitance is a linear function of thickness, with the slope corresponding the volumetric capacitance C_v . The volumetric capacitance C_v extracted from CV measurements at different LbL film thickness was 1364 F cm^{-1} (Figure 4a and Figure S6, S7) [30-32]. Using the extrapolated C_v value we now used equation (1) to calculate the mobility μ as a function of channel thickness d . This mobility is a figure of merit describing the mixed ionic/electronic conductivity of ECT materials plotted in figure 4b. In addition to μ , Figure 4b also displays the variation of maximum channel current with respect to d , showing a linear increase with thickness as expected for ECTs. The initial calculated mobility was $0.042 \text{ cm}^2 \text{ V}^{-1} \text{ s}^{-1}$ – a comparable value to that measured for state-of-the-art organic ECT materials. [33]

The mobility values however decreased asymptotically with increasing thickness approaching a stable value around $0.002 \text{ cm}^2 \text{ V}^{-1} \text{ s}^{-1}$. The decrease in mobility, which is a combined iontronic mobility, may be explained by the introduction of disorder in the orientation of the 2D flakes, and larger inter-flake distance as more materials is added in each deposition steps in the LbL process. The optimization of the film forming process is an interesting future direction for iontronic systems, and the ECT offers valuable experimental platform to this end. In the ideal scenario the mobility should be high for thin films and decrease only with a minimum asymptotic curve to stable and high values even for thicker films. These ECTs could therefore be faster. We note however that the mobility values are already good enough for many applications. The maximum ECT transconductance was also quite high with a value of 2.89 mS for the LbL MXene ECTs. Since the MXene ECTs also operated at low threshold voltages V_{th} these devices have a very low energy efficiency, and are thus suitable for low power components, such as ECRAMs for neuromorphic devices.

2.4 The origin of conductance switching in MXene: Correlating channel conductivity to electrochromism

Many mixed ionic/electronic conductors exhibit electrochromism [34], a reversible change in their optical properties due to a change in their redox state. Previous work has shown that $\text{Ti}_3\text{C}_2\text{T}_x$ MXene thin films can undergo reversible changes in optical absorption upon electrochemical cycling in acidic electrolytes (H_3PO_4 and H_2SO_4) at potentials below 1 V (with silver wire as the reference electrode) [35, 36]. Some MXenes may exhibit metal-insulator transition mediated by adsorbates induced by electrochemistry on its surface [37]. Such electrochromic effect is attributed to non-faradaic electrical double layer as well as a faradaic redox process [38]. In the case of acidic electrolytes here the main effect should be from the proton redox of Ti.

For organic ECTs, it is known that ion-electron coupling, i.e. redox reactions, leads to the formation of charge carriers (e.g., polarons and bipolarons) in the conjugated polymer backbone, resulting in a change in its bandgap, and its conductivity [6]. Here, we further correlate the phenomenon of changes in films conductance as observed in ECTs, by linking it to the optoelectrochemical behavior of 2D MXene.

To further consolidate our results, we compared the change in optical absorbance at selected wavelengths as obtained from spectroelectrochemical measurements to the drain current (Figure 4c, 4d). The increase in the current coincides with the decrease in the absorbance at reduced band (770 nm) and increase of the absorbance at wavelength 1095 nm . These data suggest that the reversible protonation of the Ti (see schematic Figure 3a) is both responsible for electrochromism as well as conductance change upon redox doping of the MXene film. This is to our knowledge a first report of this important correlation in MXene films.

In addition, reversible and irreversible ion intercalation processes, ions could physically expand the interlayer spacing which may also lead to a change in the property of the films. All these phenomena combined lead to changes in the overall optical (as probed by UV-Vis) but also long-range electronic conductivity as probed by the ECTs in a highly complex manner. The full understanding of these phenomenon is beyond the scope of this work and indeed it has taken decades to elucidate these mechanisms for a the PEDOT organic electrochemical transistors [16].

3. Conclusion

The solid-state field-effect transistor, FET, and its theories were paramount in the discovery and studies of graphene. Here we show that MXenes, a class of 2D materials beyond graphene, have mixed electronic ion properties that enable the realization of electrochemical transistors (ECTs). The current parameters of the MXene ECTs show good transconductance (0.73 mS) but low on-off ratios (1.19), these values are already state of the art for use in devices like electrochemical Random Access Memories (ECRAMs) or biosensors. Further studies of beyond graphene 2D materials within the framework of ECTs can

enable optimization of parameters such as considerably higher on-off ratios, very large channel currents, or extremely high speeds.

We further show that conductance switching data measured using ECT in combination with other in-situ ex-situ electrochemical measurements (such as UV-Vis), is a powerful tool for correlating the change in conductance to that of redox state: to our knowledge this is the first report of this important correlation for MXene films. The LbL method has the double advantage to provide a precise control over the channel thickness and to larger transconductance values with respect to spin-coating. Many future possibilities exist for MXenes ECTs as over 30 different MXenes are predicted. We foresee that even TMDs and other bandgap material can form ECTs and 2D iontronics can also comprise heterostructure films for example with mixture of MXenes and 2D TMDs.

2D ECTs can draw great inspiration and theoretical tools from the field of organic ECTs. They have the potential to considerably extend the capabilities of transistors beyond that of conducting polymer ECTs, as they have added properties such as extreme heat resistance, and tolerance for solvents, and higher conductivity for both electrons and ions than conducting polymers.

4. Method

4.1 Synthesis of MXene

MAX phase was synthesized according to our previous work [17] and powdered. MAX phase (Ti_3AlC_2) powder was delaminated in 2 g of LiF completely dissolved in 40 mL of 6 M HCl solution under constant stirring for 15 mins. This followed by addition of 2 g of MAX phase powder rate of 200 mg/min in ice bath. The etchant was maintained at 50 °C for 24 h at 550 rpm under constant stirring. The etchant was cooled to room temperature and washed several times with Millipore water until it reached a pH \approx 6. The obtained powders were dispersed in deaerated Millipore water and probe sonicated for 1 h in ice bath. The dispersed solution was centrifuged at 3500 rpm for 1 h, the supernatant collected, centrifuged at 5000 rpm, and re-dispersed in 10 mL Millipore water using vigorous shaking for 15 minutes to form the final MXene ink. The ink concentration was determined from net weight of MXene film obtained by vacuum filtration of a known volume of ink on a Celgard membrane.

4.2 MXene characterization using SEM

We produced multilayered MXene films via both spin-coated and LbL-assembled technique on Si substrates for SEM observations. Cross-sectional SEM images were obtained by field emission SEM (Hitachi S4800, Hitachi Corp., Japan).

4.3 PVA-H₂SO₄ Gel Electrolyte Synthesis

To purify absorbed air in the water, we bubbled 10 mL Milli-Q water through Ar gas for 1 h and mixed with 1 g PVA (Sigma, Mw = 89 000–98 000, 99+% hydrolyzed). The blended solution was stirred at 85 °C on a hot plate for at least 3 h until it became transparent, which means it is well-dispersed. Sequentially as-prepared solution was removed from the hot plate and cooled down until reaching to the room temperature. Afterwards, concentrated H₂SO₄ (0.6 ml) (Sigma, >97.5%) was very slowly added to the as-prepared mixed solution, followed by stirring for at least 1 h at room temperature.

4.4 ECTs fabrication

We utilized two types of MXene multilayers as redox-active channels in our study: LbL-assembled and spin-coated MXene multilayers. Prior to multilayers formations, bare glass substrates were bath-sonicated in the sequence of acetone, ethanol, and isopropyl alcohol for 20 min each. Afterwards, we patterned them with Au electrodes (channel dimensions, L = 20 μm , W = 1000 μm) using photolithography. Then, we treated O₂ plasma (Optrel GBR, Multi-stop) for 20 min to create the hydrophilic surface to facilitate the uniform coverage of 2D MXene for both cases.

To avoid any parasitic capacitances from metal/electrolyte interfaces, we coated polymethyl methacrylate (PMMA) on the source-drain Au electrode after LbL-assembled MXene formation to complete ECT devices. To prepare PMMA solution, we dissolved 1 g poly(methyl methacrylate) (Sigma, Mw \approx 996 000 by GPC, crystalline) in 10 mL Toluene (Sigma, ACS reagent, \geq 99.5%), and the mixed solution was stirred vigorously at 80-degree Celsius overnight.

For the spin-coated MXene multilayers, aqueous $\text{Ti}_3\text{C}_2\text{T}_x$ MXene solution (2 g L⁻¹) was coated at 3000 rpm for 30 seconds. This step was repeated 5, 10, or 20 times to form multilayers of increasing thickness. In the case of LbL-assembled MXene multilayers, we used tris(3-aminopropyl)amine (TAPA, Sigma) as a spacer molecule to provide the efficient interlayer chemistry. Prior to dipping the substrates, we used 3M adhesive tape to prohibit the back-side coating of the substrate during

dipping process. We treated the substrate surface by using O₂ plasma for 15 mins to modify its wetting properties and as-treated substrates were then loaded into a dipping robot (StratoSequence VI, nanoStrata Inc.). For LbL assembly setup, aqueous Ti₃C₂T_x MXene dispersion (2 g L⁻¹) and TAPA dissolved in milli-Q water (1 g L⁻¹) were used. We did 8 consecutive dipping steps including rinsing with pure milli-Q water using an automated program (StratoSmart v7.0). For the one cycle, i.e., one bi-layer formation, the substrates were firstly dipped into TAPA-dissolved solution and sequentially spun in a circle for 5 min. Subsequently, they were rinsed with the following 3 steps for 2 min each. After the formation of positive charges on the surface, the substrates were dipped and spun again in the negatively charged MXene solution for 5 min and rinsed repeatedly 3 times for 2 min. These steps were repeated for the formation of MXene multilayers. We then dried the LbL assembled films overnight in a vacuum oven at room temperature. To prevent any parasitic capacitances from undesired Au bottom electrode, we drop-casted a solution of PMMA, Sigma, Mw ~996,000 by GPC, crystalline) on the edge of dried MXene film. The gel electrolyte was then drop-casted on top of LbL-assembled MXene multilayers. Finally, Ag/AgCl pellet was dipped in the gel electrolyte to complete the electrochemical transistor configurations.

4.5 ECT data collection and characterization

We measured transistor data using a Keithly 4200A-SCS parameter analyser in air at room temperature. Data analysis was performed using Origin Pro 2020, we have smoothed the transconductance (calculated by using the equation $g_m = \partial I_D / \partial V_G$) by adjacent averaging to attenuate instrument and environment noise. We calculated the threshold voltage using ELR method. This method calculates the threshold voltage by finding the gate voltage axis intercept of the linear extrapolation of the I_D versus V_G curve at its maximum first derivative point.

4.6 In-situ spectroelectrochemistry

An ITO glass slide coated with MXene was served as the working electrode. Pt coil was used as the counter electrode and Ag/AgCl pellet was used as the reference electrode. The three-electrode cells were dipped together in the 1 M PVA-H₂SO₄ electrolytes in a standard quartz cuvette, located in the middle of beam path of an ultraviolet–visible (UV–vis) spectrophotometer (LAMBDA 750). For in-situ setup, we connected three-electrodes with cyclic voltammetry (CV) and recorded the corresponding optical absorption as a function of applied potential with a step of 0.1 V.

4.7 Impedance measurements

MXene films were deposited via LbL assembly on square gold electrodes of dimension 2 mm². For electrode fabrication, a glass wafer was cleaned via subsequent ultrasonication in soapy water for 15 minutes, basic piranha cleaning in a solution of H₂O:H₂O₂:NH₃ at around 70 °C for 5-10 minutes, and O₂ plasma for 15 mins. Gold contacts were prepared by evaporation using a custom-made paper mask [39] to form 10 nm of chromium as an adhesion layer and 50 nm of gold.

EIS measurements were performed on LbL-assembled MXene using a BioLogic VSP potentiostat. The MXene films on gold were used as the working electrode, a Ag pellet pseudo reference was used as the reference electrode, and a platinum coil as a counter electrode. The electrolyte was 1 M poly(vinyl alcohol) (PVA) in H₂SO₄, as for the ECTs. EIS data were acquired at frequencies between 100 kHz to 10 Hz at a sinus amplitude of 10 mV and a potential of -0.8 V. The capacitance was extracted by fitting the data to a modified Randles circuit model $R_s(R_p||Q)$, where R_s is the electrolyte resistance, R_p is the charge transfer resistance, and Q is a constant phase element, using ZFit (EC-Lab V11.41 software). The thickness of the films was determined in a dry state from the SEM cross section images.

4.8 CV measurements and calculation of capacitance

CV measurements were performed on LbL assembled MXene using a BioLogic VSP potentiostat with the same setup used for EIS measurements. The CV curves were obtained at scan rate of 100 mV/s. The specific capacitance $C(Fcm^{-2})$ was estimated by using equation 2[40]

$$C = \frac{1}{2kA\Delta V} \int Idv \quad (2)$$

where k is the scan rate (V s⁻¹), A is the Area of the active material (cm²), ΔV is the potential window (V) and Idv represents the area under CV curve.

Acknowledgements

M.-A acknowledges funding from ÅForsk project 18-461. J.S. acknowledges funding from Olle Engkvists stiftelse. M.H. acknowledges funding from energimyndigheten project 48489-1.

References

- [1] Novoselov K S *et al* 2004 *Science* **306** 666–9
- [2] Nicolosi V, Chhowalla M, Kanatzidis M G, Strano M S, and Coleman J N 2013 *Science* **340** 1226419
- [3] Mounet N *et al* 2018 *Nat. Nanotechnol.* **13** 246–52
- [4] Naguib M, Mochalin V N, Barsoum M W, and Gogotsi Y 2014 *Adv. Mater.* **26** 992–1005
- [5] VahidMohammadi A, Rosen J, and Gogotsi Y 2021 *Science* **372** 6547
- [6] Choi W, Choudhary N, Han G H, Park J, Akinwande D, and Lee Y H 2017 *Mater. Today* **20** 116–130
- [7] Liu Y, Duan X, Shin H-J, Park S, Huang Y, and Duan X 2021 *Nature* **591** 43–53
- [8] Nilsson D, Chen M, Kugler T, Remonen T, Armgarth M, and Berggren M 2002 *Adv. Mater.* **14** 51–4
- [9] Zeglio, E and Ingnas, O 2018 *Adv. Mater.* **30** 18800941
- [10] Rivnay J, Inal S, Sallea A, Owens R M, Berggren, M and Malliaras, G G 2018 *Nat. Rev. Mater.* **3** 17086
- [11] Bombile J H, Janik M J and Milner S T 2018 *Phys. Chem. Chem. Phys.* **20** 317–31
- [12] Friedlein J T, McLeod R R and Rivnay J 2018 *Org. Electron.* **63** 398–414
- [13] Sun H, Gerasimov J, Berggren M and Fabian S 2018 *J. Mater. Chem. C* **6** 11778–11784
- [14] Hamed M M, Forchheimer R and Ingnäs O 2007 *Nat. Mater.* **6** 357–62
- [15] Zeglio E, Rutz A L, Winkler T E, Malliaras G G and Herland A 2019 *Adv. Mater.* **31** 1806712
- [16] Gkoupidenis P, Schaefer N, Garlan B and Malliaras G G 2015 *Adv. Mater.* **27** 7176–7180
- [17] Melianas A, Kang M-A, VahidMohammadi A, Quill T J, Tian W, Gogotsi Y, Sello A and Hamed M M. 2022 *Adv. Funct. Mater.* **32** 2109970
- [18] Xu B, Zhu M, Zhang W, Zhen X, Pei Z, Xue Q, Zhi C and Shi P 2016 *Adv. Mater.* **28** 3333–3339
- [19] Tian W, VahidMohammadi A, Wang Z, Ouyang L, Beidaghi M and Hamed M M 2019 *Nat. Commun.* **10** 2558
- [20] Xu X, Zhang H, Diao Q, Zhu Y, Yang G and Ma B 2020 *J. Mater. Sci. Mater. Electron.* **31** 175–181
- [21] El-Demellawi J K, Lopatin S, Yin J, Mohammed O F and Alshareef H N 2018 *ACS nano* **12** 8485–93
- [22] Salles P, Pinto D, Hantanasirisakul K, Maleski K, Shuck C E, and Gogotsi Y 2019 *Adv. Funct. Mater.* **29** 1809223
- [23] Paulsen B D, Tybrandt K, Stavrinidou E, and Rivnay J 2020 *Nat. Mater.* **19** 13–26
- [24] Hamed M M, Tvingstedt K, Karlsson R H, Åsberg P and Ingnäs O 2009 *Nano Lett.* **9** 631–5
- [25] Nayak P, Jiang Q, Mohanraman R, Anjum D, Hedhili M N and Alshareef H N 2018 *Nanoscale* **10** 17030
- [26] Mawad, D, Molino P J, Gambhir S, Locke, I M, Officer, D L and Wallace G G 2012 *Adv. Funct. Mater.* **22** 5020–2027
- [27] Friedlein J T, Mclead R R and Rivnay J 2018 *Org. Electron.* **63** 398–414
- [28] Bernards D A and Malliaras G G 2007 *Adv. Funct. Mater.* **17** 3538–3544
- [29] Inal S, Malliaras G G and Rivnay J 2017 *Nat. Commun.* **8** 1767
- [30] Kurra N, Ahmed B, Gogotsi and Alshareef H N 2016 *Adv. Funct. Mater.* **6** 1601372
- [31] Zhang C, Kromer M P, Ascaso A S, Park S H, McEvoy N, Anasori, Gogotsi Y and Nicolosi V 2018 *Adv. Funct. Mater.* **28** 1705506
- [32] Peng Y Y, Akuzum B, Kurra N, Zhao M Q, Alhabeb M, Anasori B, Kumbur E C, Alshareef H N, Ger M D, and Gogotsi Y 2016 *Energy Environ. Sci.* **9** 2847
- [33] Sun H, Vagin M, Wang S, Creipin X, Forchheimer R, Berggren M and Fabiano, S 2018 *Adv. Mater.* **30** 1704916
- [34] Chandrasekhar P, Zay B J, Birur G C, Rawal S, Pierson E A, Kauder L and Swanson T 2002 *Adv. Funct. Mater.* **12** 95–103
- [35] Li J *et al* 2021 *Chem. Electro. Chem.* **8** 151–156
- [36] Liu Y, Jiang S P and Shao Z 2020 *Mater. Today Adv.* **7** 100072
- [37] Fredrickson K D, Anasori B, Seh Z W, Gogotsi Y, and Vojvodic A 2016 *J. Phys. Chem. C* **120** 28432–440
- [38] Zhan C, Naguib M, Lukatskaya M, Kent P R, Gogotsi Y, and Jiang D E 2018 *J. Phys. Chem* **9** 1223–8
- [39] Nik F E, matthiesen I, Herland A and Winkler T 2020 *Micromechanics* **11(7)** 676
- [40] Zhang W, Tan Y, Gao Y, Wu J, Tang B, and Zhao J 2014 *RSC Adv.* **4** 27800–27804

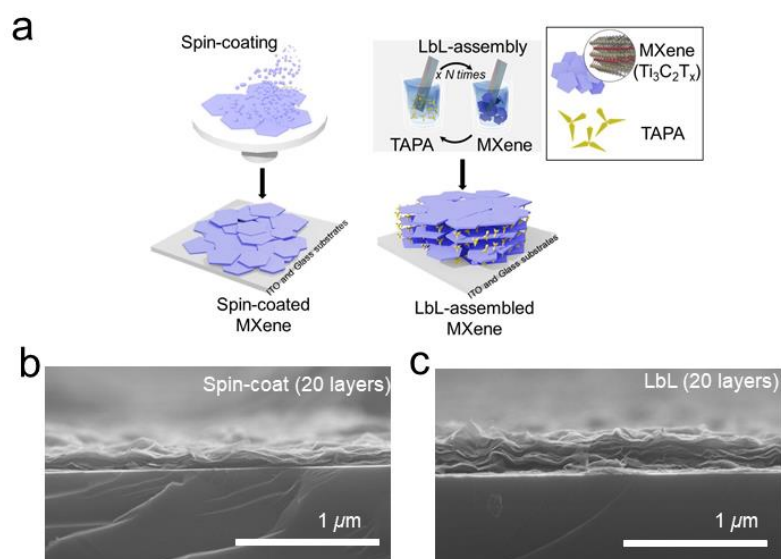


Figure 1. (a) Schematic diagram showing fabrication of MXene films using spin-coating, or using LbL self-assembly. SEM images of MXene films fabricated with (b) 20 layers of spin-coating and (c) 20 layers of LbL coating.

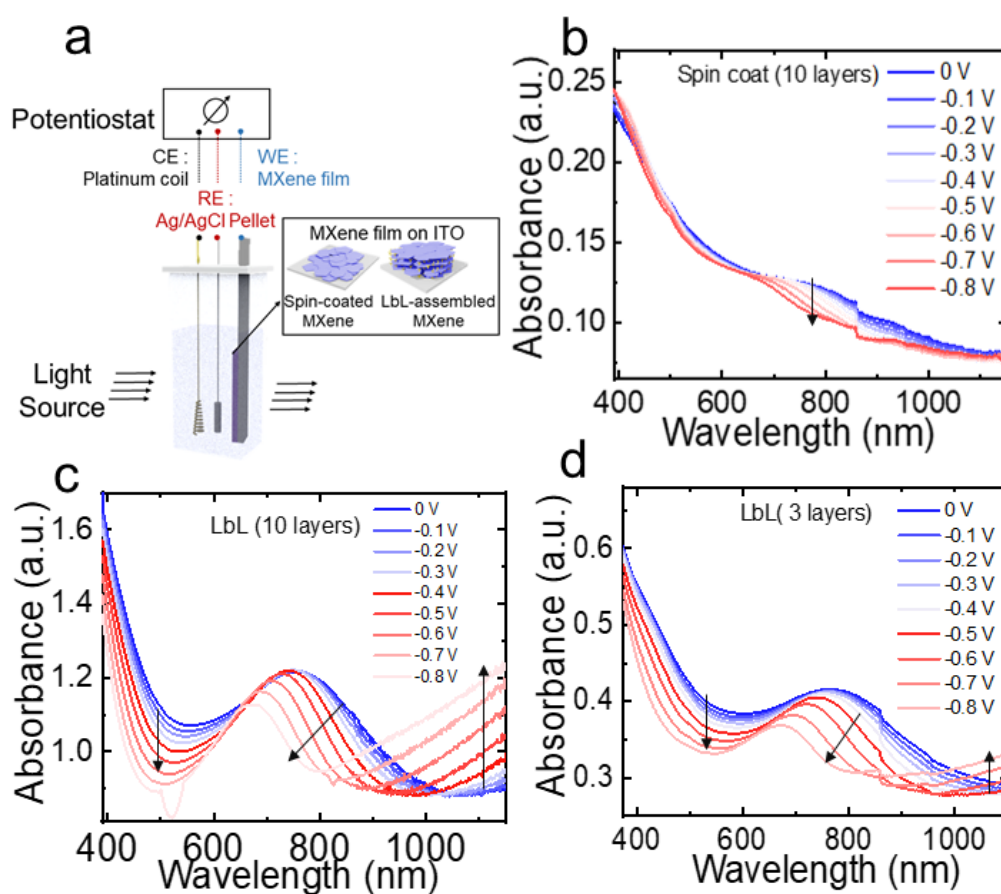


Figure 2. (a) Schematic diagram of the in-situ spectroelectrochemical measurement setup. UV-vis spectroelectrochemical measurements of (b) spin-coated and LbL-assembled (c) 10 Layers (d) 3 Layers MXene films at decreasing redox doping voltages from 0 to -0.8 V with steps of 0.1 V.

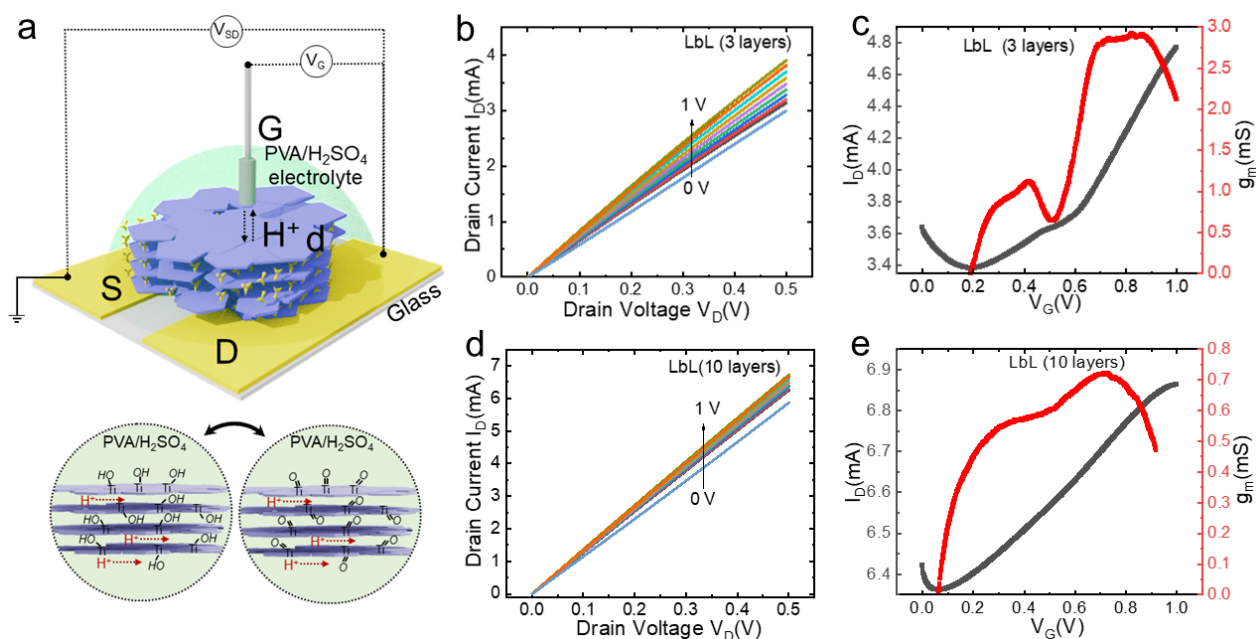


Figure 3. (a) Schematic representation of the ECT device. Electrical characteristics of MXene ECTs having LbL assembled MXene films as channels (b, d) Output curves for different ECTs measured for gate voltages ranging from 0 to 1 V (c, e) Corresponding transfer curves and calculated transconductance values measured at $V_D = 0.5$ V.

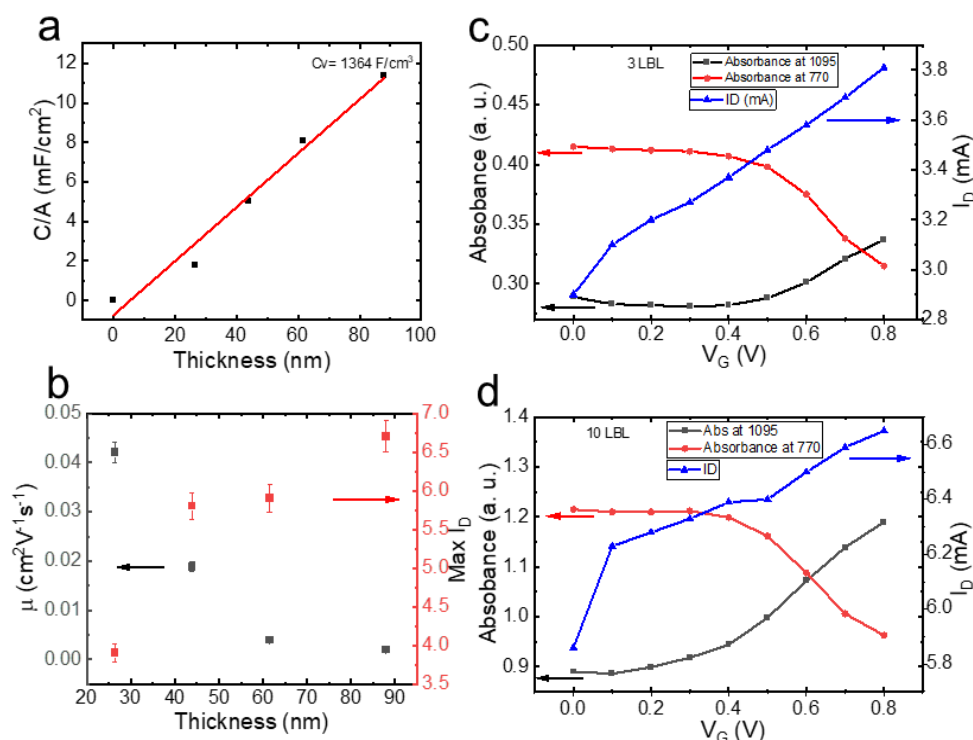


Figure 4. (a) Volumetric capacitance C_v measured for LbL film with 3, 5, 7 and 10 bi-layers showing a linear correlation (b) A comparison of mobility and maximum current for LbL assembled MXene with varying thickness. ECT Drain current vs. UV-vis absorbance at 1095 nm and 770 nm measured at different redox potentials (vs. Ag/AgCl) for the films: (c) LbL 3 layers (d) LbL 10 layers

Supplementary Information

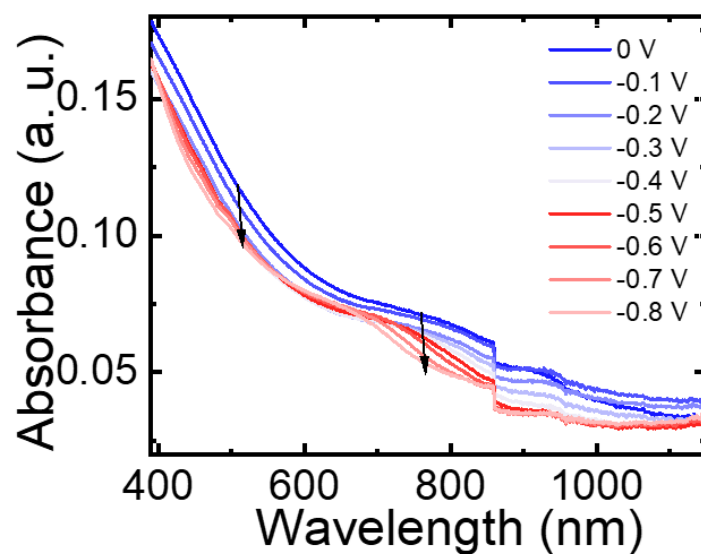


Figure S1. UV-vis spectroelectrochemical measurements of spin coated MXene (5 Layers).

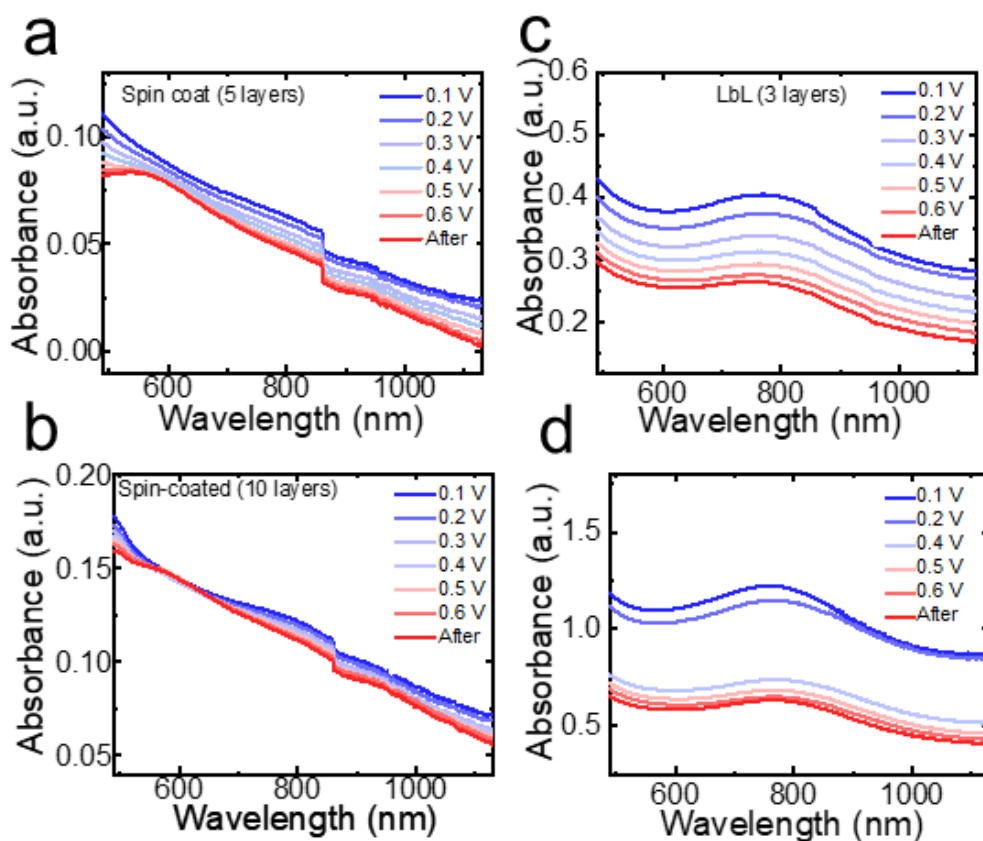


Figure S2. UV-vis spectral absorbance for oxidation of (a) Spin coated (5 layers) (b) Spin coated (10 layers) (c) LbL (3 layers) (d) LbL (10 layers).

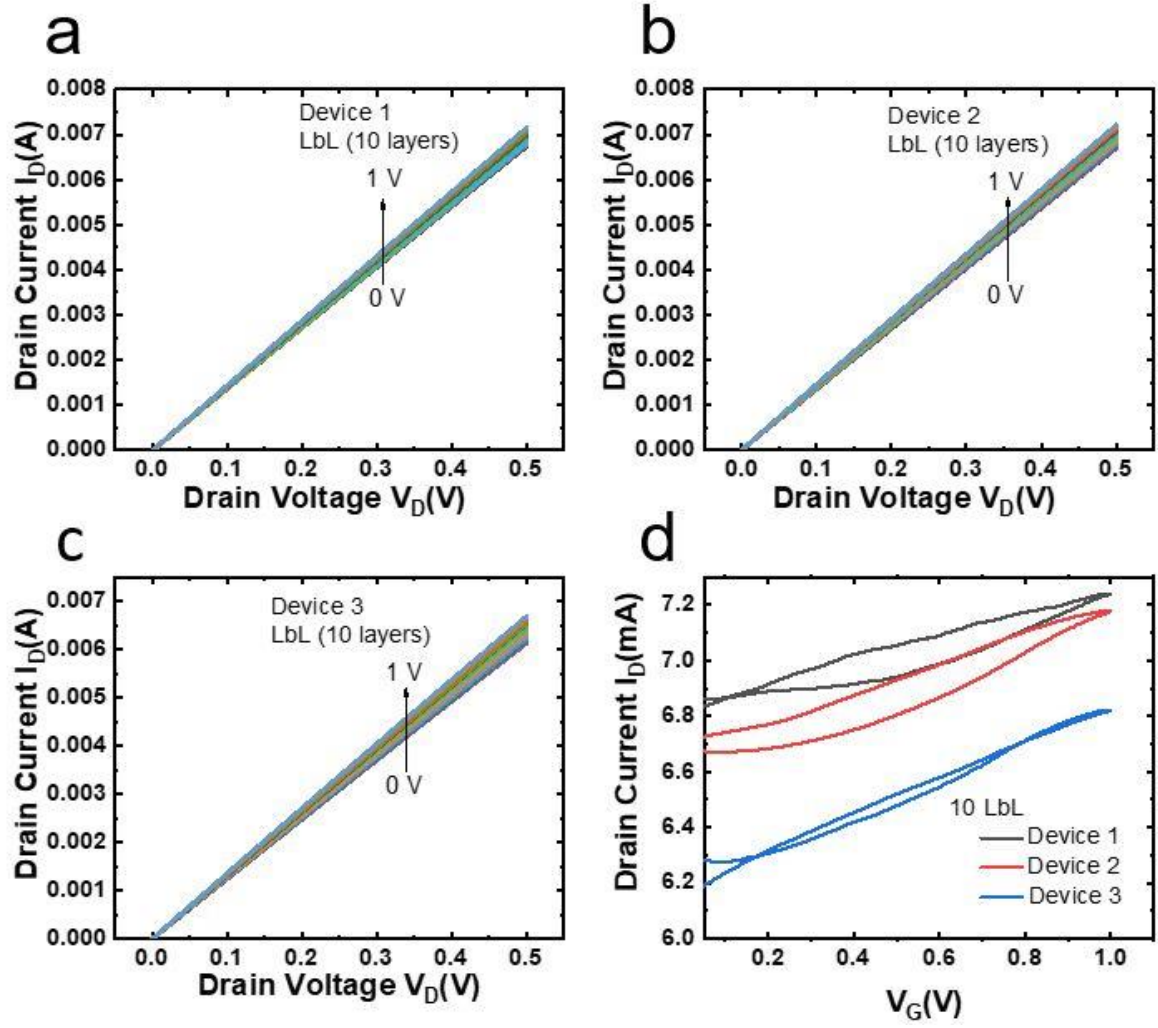


Figure S3. Device to device variability: Electrical characteristics of MXene ECT devices having LbL (10 Layers) assembled MXene films as channels. (a, b, c) Output curves for various ECT devices measured for gate voltages ranging from 0 to 1 V. (d) A comparison of corresponding transfer curves for devices 1, 2 and 3.

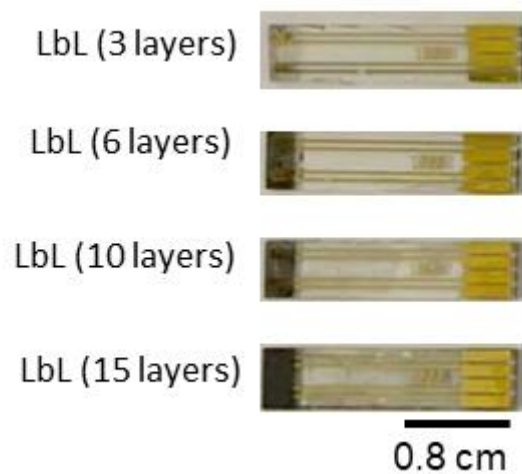


Figure S4. Photos of ECTs with LbL films of various thickness.

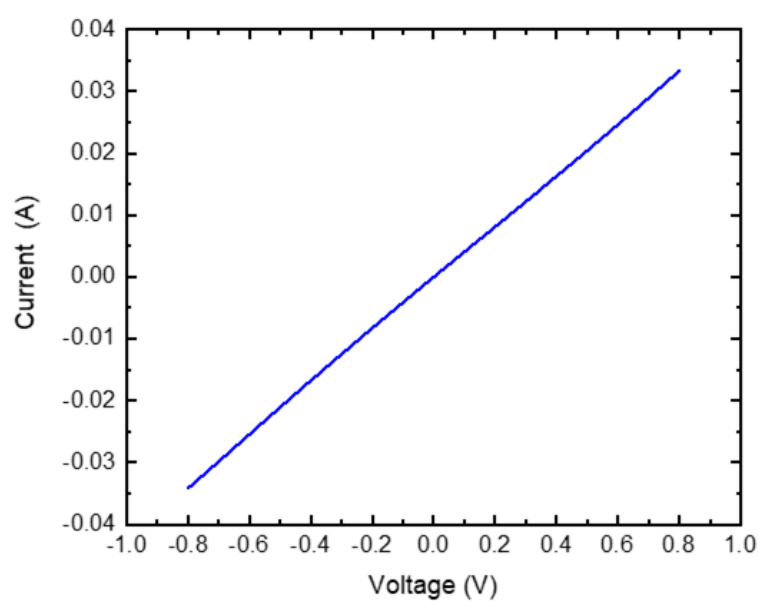


Figure S5. IV data for LbL MXene dry films in between S-D in an ECT.

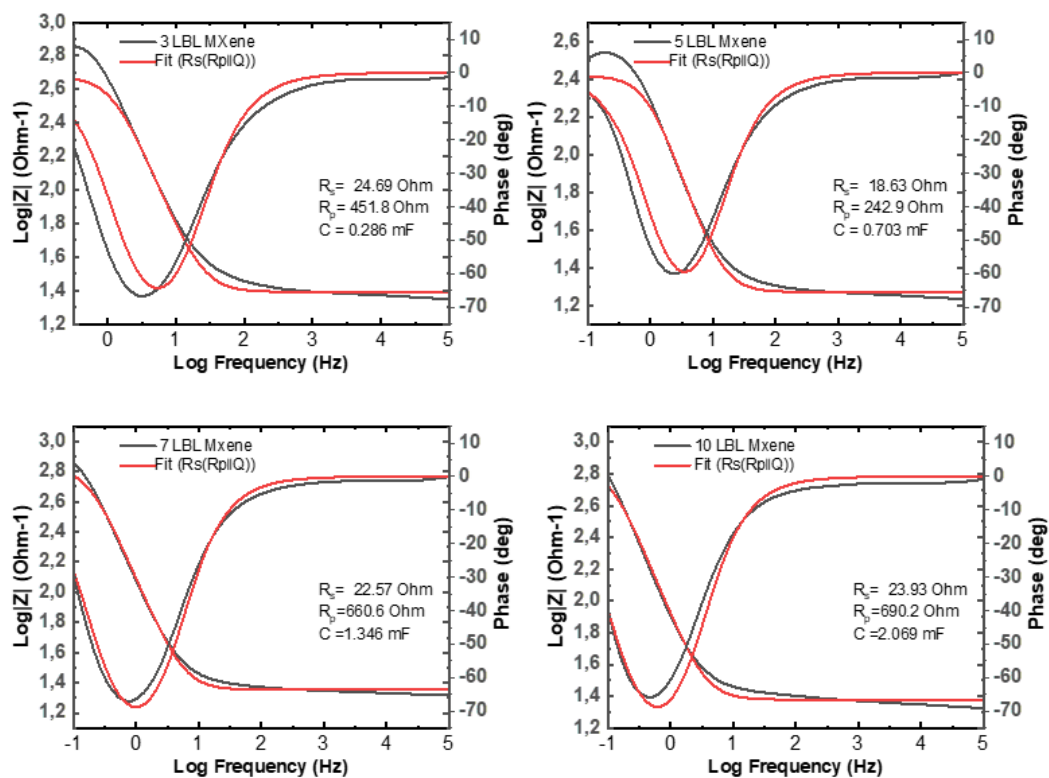


Figure S6. EIS Bode plot of 3, 5, 7 and 10 layers of MXene prepared by layer-by-layer technique.

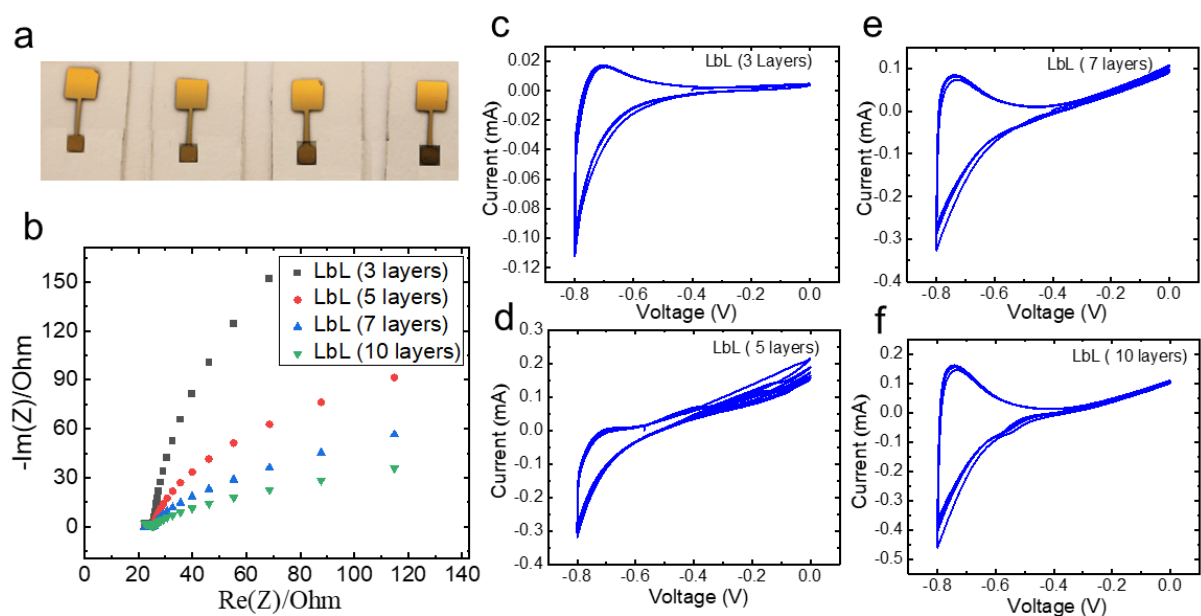


Figure S7. (a) Electrodes used for impedance measurements (b) EIS Nyquist plot and cyclic voltammograms of (c) 3, (d) 5, (e) 7 and (f) 10 layers of MXene prepared by layer by layer technique. All measurements were performed using a three-electrode setup with a Ag/AgCl pellet acting as a pseudo reference electrode.

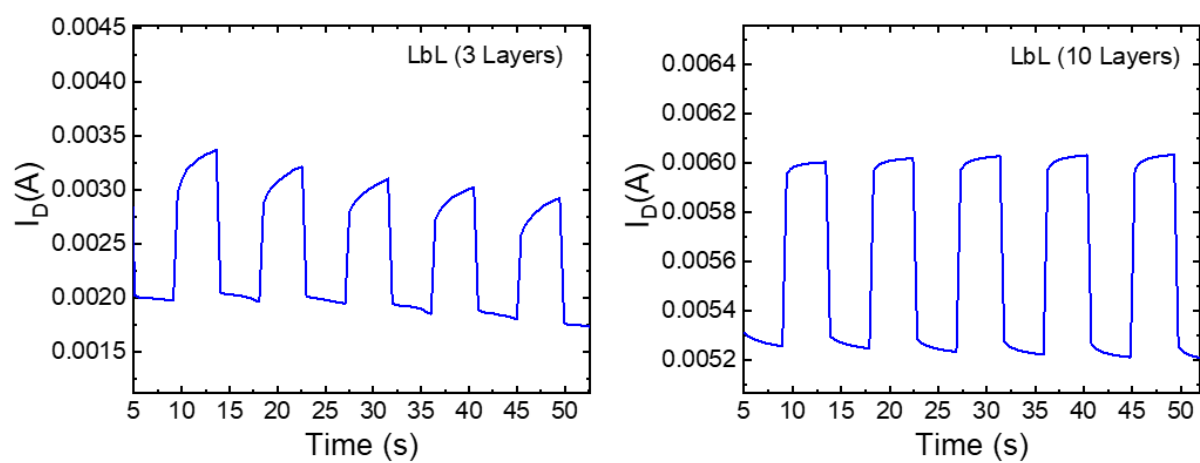


Figure S8. The dynamic switching characteristics of LbL (3 Layers) and LbL (10 Layers)